AGU PUBLICATIONS

JGR

Journal of Geophysical Research: Space Physics

RESEARCH ARTICLE

10.1002/2014JA019836

Key Points:
- The Weimer [1996] model works quite well for driving the plasmasphere
- A saturation technique for determining the plasmapause location in introduced
- Plasmapause determined by IMAGE may not be the steepest gradient in density

Correspondence to:
A. J. Ridley,
ridley@umich.edu

Citation:
Ridley, A. J., A. M. Dodger, and M. W. Liemohn (2014), Exploring the efficacy of different electric field models in driving a model of the plasmasphere, *J. Geophys. Res. Space Physics*, *119*, 4621–4638, doi:10.1002/2014JA019836.

Received 29 JAN 2014
Accepted 29 MAY 2014
Accepted article online 3 JUN 2014
Published online 20 JUN 2014

Exploring the efficacy of different electric field models in driving a model of the plasmasphere

A. J. Ridley[1], A. M. Dodger[1], and M. W. Liemohn[1]

[1]Department of Atmospheric, Oceanic, and Space Science, University of Michigan, Ann Arbor, Michigan, USA

Abstract The dynamics of the plasmasphere are strongly controlled by the inner magnetospheric electric field. In order to capture realistically the erosion of the nightside plasmapause and the formation of the drainage plume in a model of the plasmasphere, the electric field must be accurate. This study investigates how well five different electric field models drive the Dynamic Global Core Plasma Model during eight storm periods. The five electric field models are the Volland-Stern analytic formula with Maynard-Chen *Kp* dependence, two versions of the Weimer statistical models (96 and 05), and two versions of the Assimilative Mapping of Ionospheric Electrodynamics (AMIE) technique using magnetometer and DMSP satellite data. Manually extracted plasmapause locations from images taken by the EUV instrument on the Imager for Magnetopause-to-Aurora Global Exploration (IMAGE) satellite, as described by Goldstein et al. (2005), were compared to the simulation results throughout the main phase of the eight events. Three methods of calculating the plasmapause were employed to determine the best fit to EUV data, using the maximum gradient, a constant density contour (fit method), and the location in which the modeled density fell significantly below the specified saturation density for the given radial position (saturation method). It was found that the simulations driven by the Weimer (1996) model produced the best fit overall and that the fit and saturation methods worked best for matching the model results to the observations.

1. Introduction

The plasmasphere is a toroidal region of the inner magnetosphere composed of cold (~1 to 2 eV), dense plasma of ionospheric origin that is trapped along the geomagnetic field lines [e.g., *Lemaire and Gringauz*, 1998]. In ideal quiet times, the plasmaspheric flux tubes fill to an equilibrium, where the flow of ionospheric plasma up field lines on the dayside is balanced by plasma flowing down field lines on the nightside. This cold, dense plasma convects around the Earth, influenced by the convection and corotation electric fields, forming a stable outer boundary known as the plasmapause [*Gringauz et al.*, 1961; *Carpenter*, 1963; *Carpenter and Park*, 1973]. At the plasmapause, field lines transition from the corotational-dominated motion around the Earth to the globally sunward magnetospheric convection motion. This produces a sharp drop in electron densities, from the order of 1000 to 100 cm^{-3} to that of 10 to 1 cm^{-3} [*Lemaire and Gringauz*, 1998]. During geomagnetic disturbances, convection electric fields increase, leading to an erosion of the outer layers of the plasmasphere and an inward motion of the plasmapause, taking place over the course of a few hours [e.g., *Carpenter and Lemaire*, 1997].

The location of the plasmapause is vital for understanding the interaction of the ring current and radiation belt regions, which overlap the plasmasphere spatially but contain higher-energy particle populations. ULF waves can transfer energy to radiation belt electrons via resonant oscillations, but the penetration of these waves is a function of the local plasma mass density [*Shprits et al.*, 2006; *Ozeke and Mann*, 2008; *Zong et al.*, 2009]. ELF/VLF waves, which are excited both inside and outside the plasmapause, can resonantly interact with radiation belt electrons on their gyration time scale, but the nature of this interaction is highly dependent on the local plasma density [e.g., *Kennel and Petschek*, 1966; *Lyons and Thorne*, 1973; *Summers et al.*, 1998].

The plasmapause undergoes significant distortion in shape during plasmasphere erosion, due to the evolution of the dayside drainage plume [e.g., *Grebowsky*, 1970; *Horwitz et al.*, 1986; *Moldwin et al.*, 2003a; *Spasojević*, 2003]. The drainage plume is a high-density (sometimes exceeding 100 cm^{-3}) column of plasma, flowing from the plasmasphere to the dayside reconnection site that depending on storm intensity can last for as many as 4 days [*Carpenter and Lemaire*, 1997; *Borovsky and Denton*, 2008]. Recent work has indicated

that during storms, the plume can mass load the dayside reconnection site, leading to a decoupling of the solar wind and the magnetosphere [*Foster*, 2004; *Borovsky and Denton*, 2006].

Because the structure and dynamics of the plasmasphere are dominated by convection, an understanding of the global electric field is required. However, there is no method available to routinely obtain the full global-electric-field pattern, and thus, simulation is required. There are numerous models that attempt to provide a description of the global potential patterns (assuming no inductive electric field), and these models scale dramatically with regards to complexity. At the low-complexity end are models that make use of two-cell convection patterns that respond to simple geomagnetic indices such as *Kp* [*Volland*, 1973; *Stern*, 1975]. More advanced models make use of statistical studies of ground-based radars [*Foster et al.*, 1986; *Sojka et al.*, 1986] or low-altitude satellites [*Weimer*, 1996, 2005] to characterize global potential patterns based on solar driving conditions. Recently, *Matsui et al.* [2010] used Cluster data to improve an empirical model of the inner magnetospheric electric field during storms. There are also models that make use of assimilative methods, taking in data from multiple ground-based and space-based data sources [*Richmond and Kamide*, 1988], making the results dependent on the quantity and variety of the input data.

Previous studies have examined the effect of different driving electric field models on inner magnetospheric physics. For example, *Ober et al.* [1997] and *Goldstein et al.* [2005] have made use of numerical studies of the plasmasphere driven by a single electric field model. *Liemohn et al.* [2004] examined the result of varying the driving electric fields for a single event, finding that *Weimer* [1996] specified electric fields and fields generated self-consistently by a ring current model are superior to an analytical two-cell convection pattern in regard to describing storm time development of plasma morphology. Similarly, *Liemohn et al.* [2006] found, for two storm intervals, that the Volland-Stern field was almost as good as a self-consistent electric field at matching the plasmaspheric data but was less consistent in its accuracy of specific measurements. *Pierrard et al.* [2008] also attempted to compare multiple driving electric field models, though that study focused on finding the plasmapause by employing a pair of formation theories as opposed to identifying the measured characteristics of the plasmapause as in *Liemohn et al.* [2004], which produced consistent results for the shared storm in the two studies.

The study reported on here examined the density structure of the modeled plasmasphere as a result of five different electric field descriptions: a simple *Kp*-driven Volland-Stern model [*Volland*, 1973; *Stern*, 1975] with *Kp* dependence as found by *Maynard and Chen* [1975], two variations of the *Weimer* [1996, 2005] empirical model, and the Assimilative Mapping of Ionospheric Electrodynamics (AMIE) [*Richmond and Kamide*, 1988; *Ridley and Kihn*, 2004], which used ground-based magnetometers and a combination of magnetometers and Defense Meteorological Satellite Program (DMSP) data measurements [*Rich and Hairston*, 1994]. The study examined a total of eight storms in 2001, with the storm on 21 October 2001 chosen to be described in depth for its abundance of valid IMAGE EUV data for comparison.

2. Numerical Approach

This study used results from the Dynamic Global Core Plasma Model (DGCPM) [*Ober et al.*, 1997], which solves a continuity equation to calculate the content of cold thermal ions, with the source being the dayside ionosphere and sinks being both the nightside ionosphere and the model boundary at 10 R_E. The plasmaspheric filling rate on the dayside is determined by the difference between the density in the given cell and the saturation density as specified by *Carpenter and Anderson* [1992], using refilling time scales dependent on both magnetic local time (MLT) and latitude similar to those discussed in *Rasmussen et al.* [1993] and *Dent et al.* [2006]. The plasma is convected in the DGCPM using a second-order upwind scheme with a Superbee limiter. While being fundamentally the same model as used in earlier studies by *Ober et al.* [1997] and *Liemohn et al.* [2004], the current version has undergone significant modification to be fully integrated into the Space Weather Modeling Framework (SWMF) [*Tóth et al.*, 2005, 2012] and to fix a numerical issue that caused erroneous filling during some specific electric field conditions at the outer boundary.

A total of five different choices of the inner magnetospheric electric fields were selected for this study. The first option was a simple Volland-Stern electric field [*Volland*, 1973; *Stern*, 1975], with the maximum and minimum potentials being calculated based on the *Kp* index [*Maynard and Chen*, 1975]. The second and third options were to map the potential distribution provided by the Weimer empirical models [*Weimer*,

1996, 2005] into the inner magnetospheric equatorial plane using a dipole magnetic field (hereafter simply referred to as W96 and W05). The forth and fifth methods make use of the AMIE method [*Richmond and Kamide*, 1988; *Ridley and Kihn*, 2004] to produce electric potential maps of the ionosphere using only ground-based magnetometer data (hereafter simply AMIE-MAG) and a combination of magnetometer and DMSP driftmeter data (hereafter simply AMIE-DMSP). These maps were also mapped to the magnetospheric equatorial plane using a dipole magnetic field. With the exception of the Volland-Stern potentials (which can be calculated within a subroutine in DGCPM itself), all of these potentials are passed to DGCPM through coupling with the Ridley Ionosphere Model within the SWMF system [*Tóth et al.*, 2005]. These potential patterns are specified on a grid in the ionosphere and mapped out to the equatorial magnetosphere. The Weimer and AMIE patterns extend to subauroral latitudes, which can map to the plasmasphere, and are therefore capable of specifying the electric potential conditions in the plasmasphere.

The model results were compared with data obtained by the Imager for Magnetopause-to-Aurora Global Exploration (IMAGE) mission, specifically the extreme ultraviolet imager (EUV) instrument [*Sandel et al.*, 2000]. Plasmapause locations were manually extracted every 10 min from the EUV images (from a monochromatic color-scale image after mapping the data to the equatorial plane) when the satellite was near apogee, as described by *Goldstein et al.* [2005]. These extracted points were made publicly available and were used in this study.

The plasmasphere is composed of approximately 80% H^+ ions, 20% He^+, and a very small amount of O^+ [e.g., *Horwitz et al.*, 1990]. H^+ cannot be optically imaged due to the lack of emissions, so imagers must rely on emissions from He^+. The EUV instrument took advantage of the 30.4 nm resonantly scattered emission to produce global maps of the plasmasphere. The plasmasphere is optically thin to this emission, and all other sources are negligible in this band. It has been shown that the He^+ and the mass density plasmapause are normally detected close to the same location [*Moldwin et al.*, 2003b; *Goldstein*, 2003; *Dent et al.*, 2006; *Darrouzet et al.*, 2008; *Obana et al.*, 2010], though a more recent study indicated that the relative abundances vary during storm events, which can cause errors when doing a direct comparison between the IMAGE EUV data and DGCPM model results [*Sandel*, 2011].

For each run, the location of the plasmapause was calculated within the model data using three different methods. The first of these was the gradient method (shorthand "GRAD"), which employed the commonly used method of identifying the peak gradient of the natural log of the density in the radial direction for each longitude. As the plasmapause is a rapid decrease in density over a short distance [e.g., *Gringauz et al.*, 1961; *Carpenter and Park*, 1973; *Moldwin*, 1997], the method should, by definition, have identified the plasmapause. An issue with this method was found during storm time as the plume formed: as the plasmasphere was eroded on the nightside and moved around to the dayside, the density gradients on the nightside became steeper, while the gradients on the dayside became more shallow. This meant that, at times, the plasmapause on the dayside could not be found within the model, while there was a plasmapause identified in the EUV data. This could be due to two different reasons: (1) the model is inherently flawed and produced too small a density gradient or (2) the plasmapause identification method used with the model does not match the plasmapause identification method used in *Goldstein et al.* [2005] to extract the points. Without further study, it is impossible to determine which may be the case. Due to this, a pair of alternative methods were explored.

The second method used the EUV-extracted plasmapause points (as described by *Goldstein et al.* [2005]) to determine an optimum threshold density for the plasmapause location (shorthand "FIT"). DGCPM densities were calculated at the EUV-extracted plasmapause points, and the average density across all of these points for the entire event was found. The position of this specific density contour over the course of the storm was then recorded as the plasmapause.

The third method made use of the saturation density function described in *Carpenter and Anderson* [1992] and implemented in DGCPM. The density values were compared to the saturation density value, and the first point radially from the Earth where the density values fell below 95% of the saturation density was identified as the plasmapause. The process was restricted to density values between 1000 and 1 cm^{-3}, as the plasmapause is not typically found outside of these values. If no point was within the bounds, no plasmapause was recorded, though in practice there were very few times when this occurred. The times where this did occur were often within the drainage plume, such that the density was always above the saturation level.

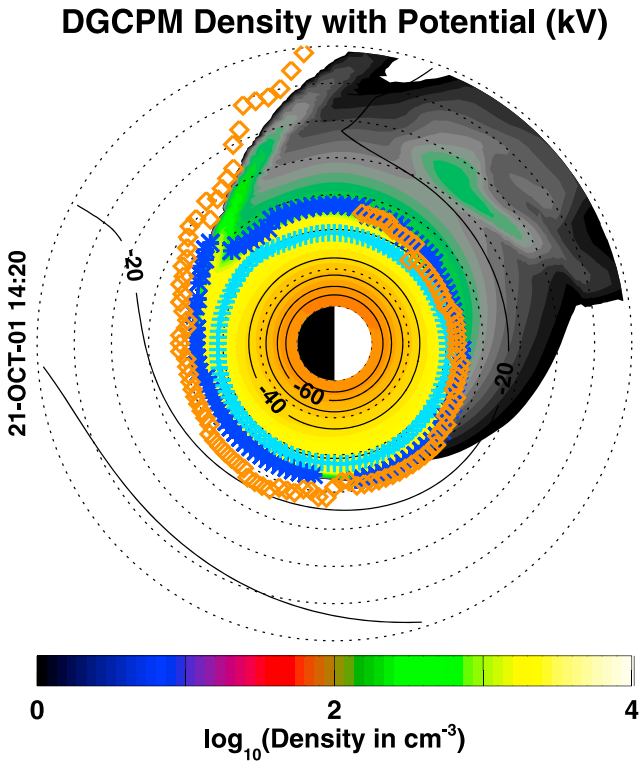

Figure 1. A single DGCPM density contour plot with plasmapause points indicating the values found by the "Grad" (orange), "Fit" (blue green), and "Sat" (dark blue) methods. The Sun is to the right, with dawn being at the bottom. The plasmaspheric potential (in kV) is shown as line contours.

A comparison of calculated plasmapauses from the three methods is shown in Figure 1. Key points to observe are that the gradient method (orange) frequently produced the furthest radial plasmapause, while the fitted method (blue green) produced the most interior plasmapause. This also meant that the gradient method had the largest response to plasmaspheric erosion during storm events, while the fitted methods had the least. Interestingly, the saturation and gradient methods corresponded for much of the plasmasphere, though they deviated in the postdusk region, where there was a bulge of lower density plasma.

3. Single-Event Analysis

On 21 October 2001, the magnetosphere experienced an intense geomagnetic storm driven by a single coronal mass ejection (CME). The plasmapause during this event was also explored by *Liemohn et al.* [2006]. An overview of the event showing critical data for storm characterization, and modeling is shown in Figure 2. The storm peak occurred at 2128 UT on 21 October, as indicated by a peak *Dst* at −186 nT. The storm intensity was still large on the following day. Solar wind and interplanetary magnetic field (IMF) measurements were taken upstream by the Advanced Composition Explorer (ACE) [*Stone et al.*, 1998]. The ACE data were lagged by an average of approximately 50.4 min on the 21st, using a simple ballistic propagation method [e.g., *Ridley*, 2000], given the average ACE satellite position of $(X, Y, Z) = (221, 4, -26)$ *Re*. Upon CME arrival, the solar wind velocity and density increased dramatically, with the velocity doubling and densities reaching as high as 60 cm^{-3} at storm peak. This increase in speed led to a decrease in the time delay between ACE and the magnetopause to a daily averaged value of approximately 35.3 min (the position was almost exactly the same). The CME also contained a strong southward IMF B_z (about −30 nT), which caused the increase in the cross-inner-magnetospheric potential (CIMP, analogous to the commonly used cross-polar-cap potential, which is defined as the maximum polar cap potential minus the minimum polar cap potential, but in this case it is only considering the potential in the magnetospheric equatorial plane at radial distances less than 10 R_E) during the storm.

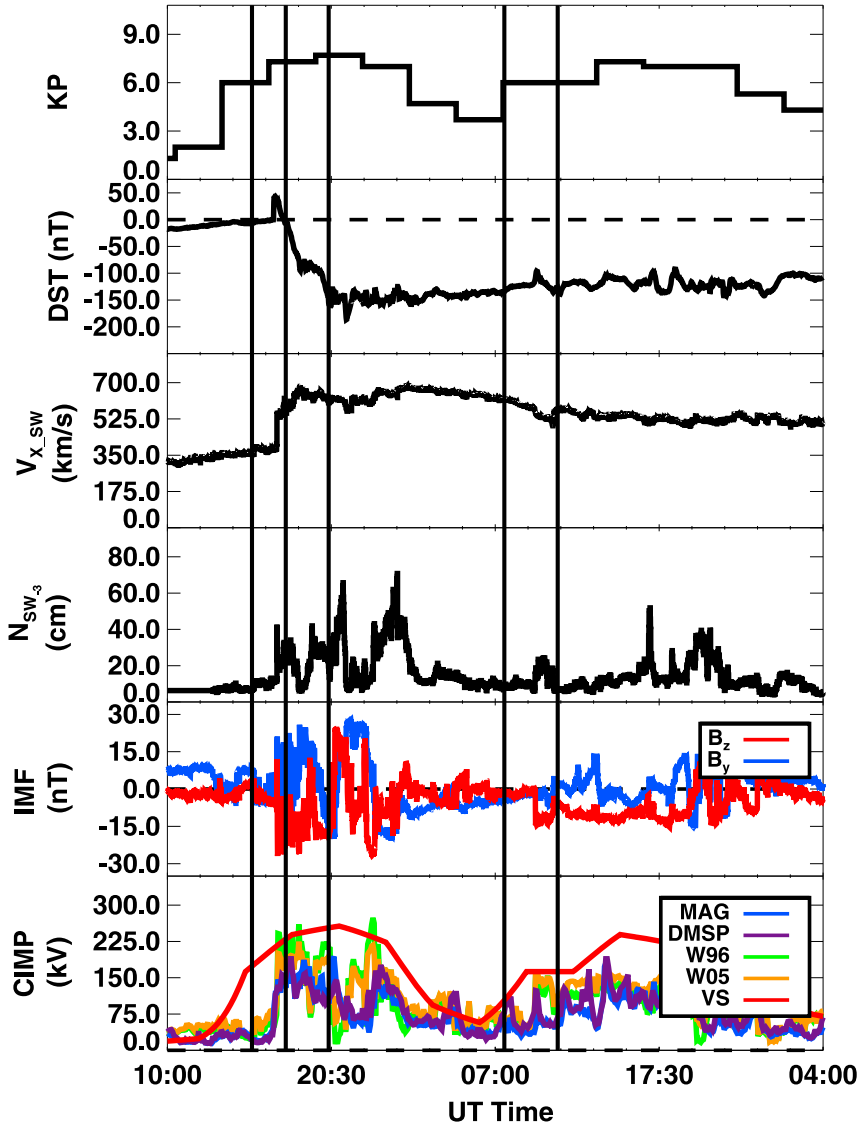

Figure 2. Summary overview of the 21–22 October 2001 storm event: (1) *Kp* 3 h geomagnetic disturbance index, (2) *Dst* index determined by AMIE, (3) solar wind velocity, (4) solar wind number density, 5) interplanetary magnetic field *Y* and *Z* components (GSM coordinates), and (6) cross-inner-magnetospheric potential (CIMP) calculated from the model simulations.

3.1. Electric Fields

Figure 3 shows the potential contours that served as drivers of DGCPM at select time periods indicated by vertical lines in Figure 2. Figure 3 (first row) shows the potential values calculated just before the storm using each of the electric field models. With the exception of the Volland-Stern model, each plot shows mild potential patterns that indicate mostly corotational flow without significant convection. The Volland-Stern distribution was that of a moderate storm, due to the 3 h cadence of the *Kp* index, which led to a strong sunward convection well before any other model.

Moving into the storm's main phase (Figure 3, second row), a strong convection pattern occurred. Significant differences in the potential patterns existed. Both AMIE results show a region around dusk in which the flow doubles back on itself (seen as a contour line that circles from the dayside past dusk and then loops around to return to the dayside in the AMIE DMSP column). Both the W96 and W05 models showed this flow reversal feature, but in neither was it as intense as in the AMIE variations. While this strong convection was maintained in the W96 and W05 simulations in Figure 3 (third row), nearly 3 h later, the AMIE patterns indicated

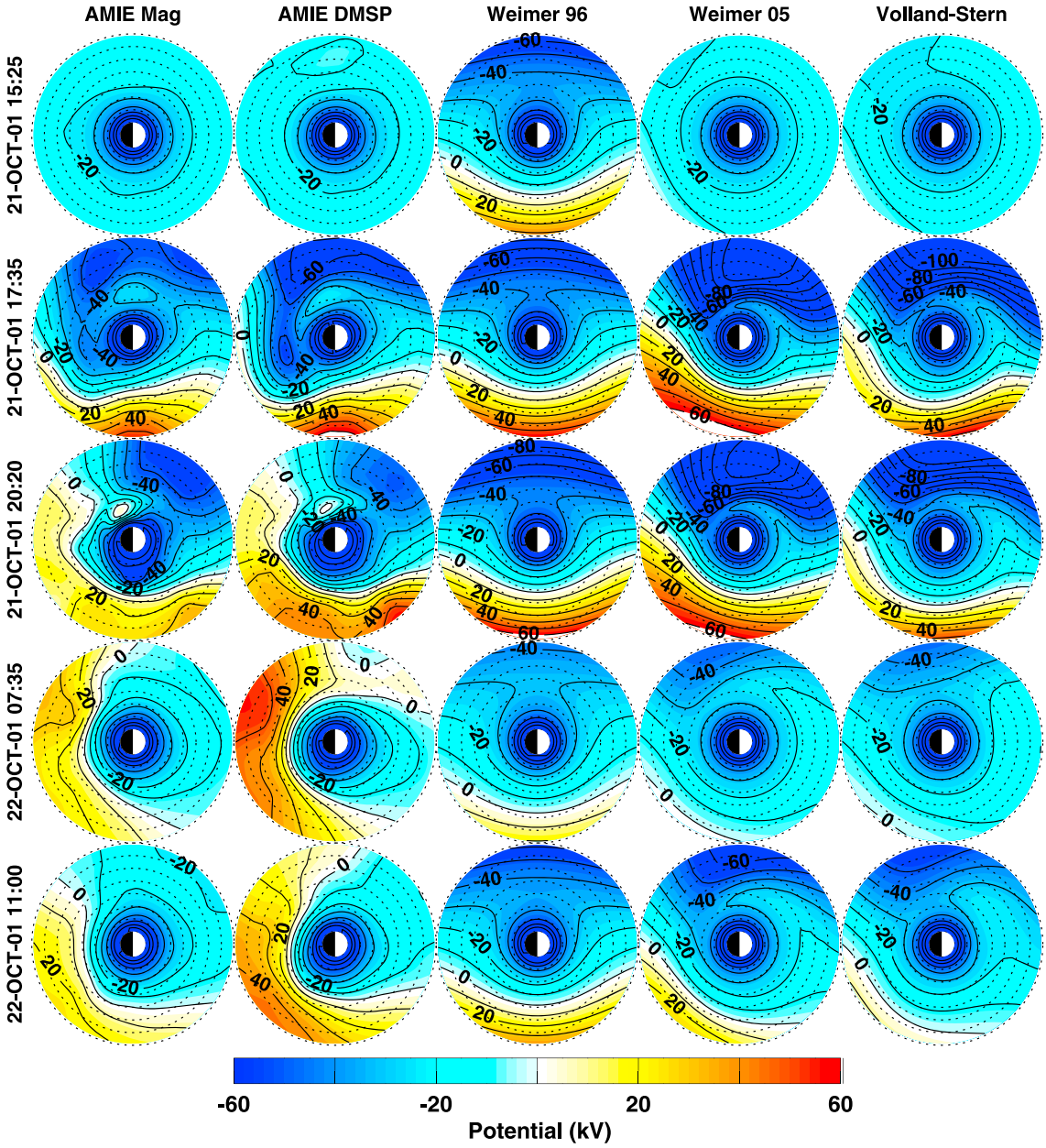

Figure 3. (first to fifth rows) Potential contours, including corotation, produced by the five electric field models at the times indicated in Figure 2. On each plot, the Sun is to the right, with dawn at the bottom. From left to right, models are AMIE-MAG, AMIE-DMSP, W96, W05, and VS.

a more "confused" potential distribution, with significant bulges in the contours. Convection in the AMIE patterns had decreased, leading to weaker erosion while the storm was still approaching its peak.

Figure 3 (fourth and fifth rows) indicates times in which an eroded plasmasphere would be expected. The potential differences across the plasmasphere (in most cases) were significantly smaller than during the storm onset. The AMIE patterns indicate a potential gradient that had reoriented from dusk to dawn to day to night, which caused a dawnward flow at the edge of the plasmasphere. Using DMSP data as well as magnetometer data (i.e., column two) showed even greater potential differences and thus greater plasma flow. The Weimer potentials, on the other hand, showed some variation in the orientation of the contours, but the flow was still decidedly sunward. Figure 3 (fifth row) shows AMIE potential differences returning to a more common dusk-to-dawn configuration but still tilted more significantly than any other model.

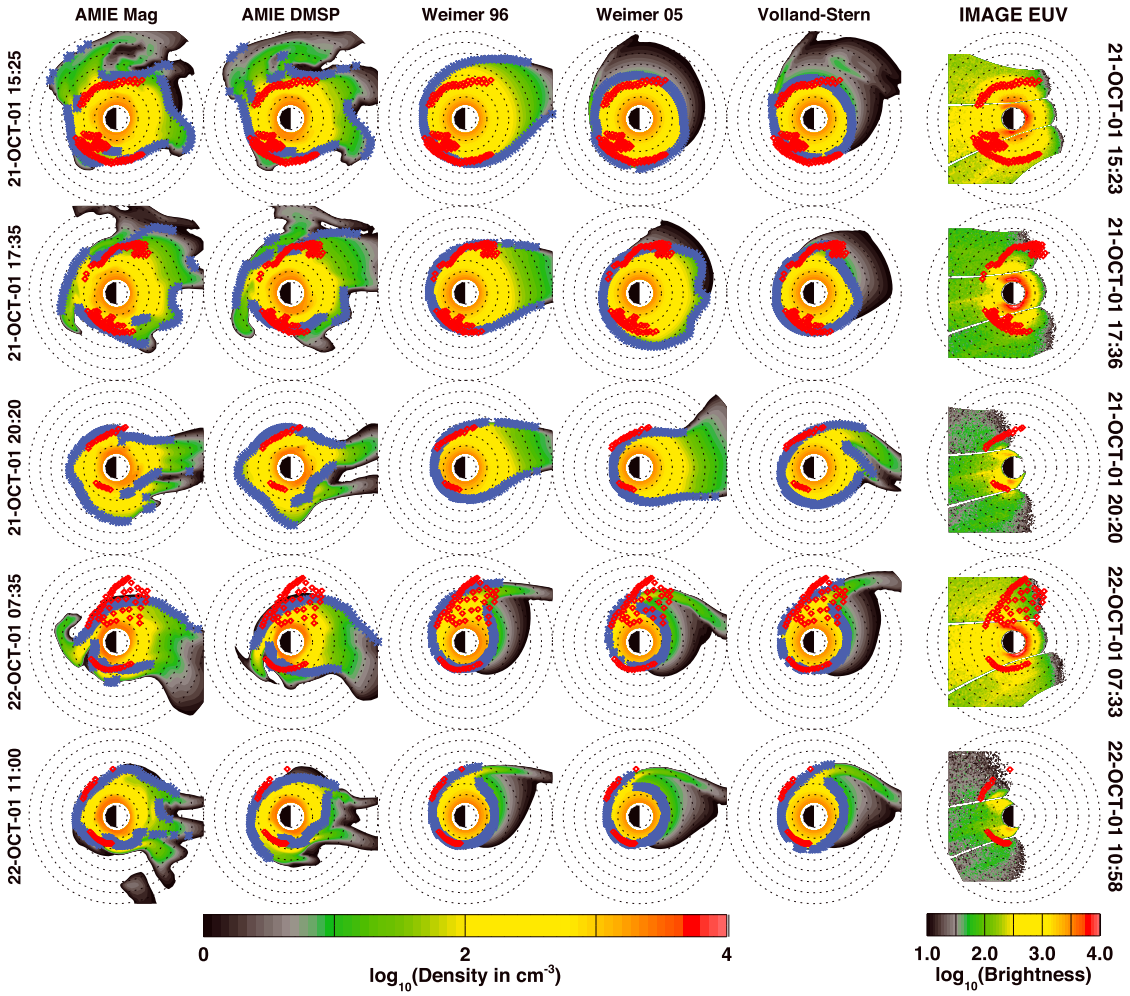

Figure 4. (first to sixth rows) Equatorial electron number density contours produced by the five electric-field models at the indicated times on Figure 2. Dark blue dots on the contours indicate the model-calculated plasmapause points using the saturation method, with the red diamonds indicating the IMAGE EUV plasmapause points extracted as discussed in *Goldstein et al.* [2005]. On each plot, the Sun is to the right, with dawn at the bottom. From left to right, models are AMIE-MAG, AMIE-DMSP, W96, W05, and VS. The final column shows the IMAGE EUV data mapped to the equatorial plane.

3.2. Density Contours

Figure 4 shows the equatorial electron number density distribution in the plasmasphere that resulted from the model being driven by the different potential models as described above and demonstrated in Figure 3. The density contour varies from 10,000 to 1 cm^{-3} to highlight both the interior plasmasphere and the exterior plasma trough, which was below the observational limit of the EUV instrument of approximately 40 cm^{-3} [*Goldstein*, 2003]. Red diamonds on the plot indicate extracted plasmapause points from EUV data as described in *Goldstein et al.* [2005], while the dark blue dots indicate the calculated plasmapause locations from the DGCPM model via the saturation method mentioned above.

The last column in this figure shows the IMAGE EUV data mapped to the equatorial plane by taking each pixel's pierce point through the equator and assigning the brightness to that specific L shell and magnetic local time. This is an extremely simplistic description, but the studies by *Sandel et al.* [2003] and *Roelof and Skinner* [2000] provide a more thorough description of the mapping. The brightness changed as a function of time because the satellite was moving such that the distance to the plasmapause was changing. The EUV data are included simply for reference.

Figure 4 (first row) shows a prestorm plasmasphere in the case of the AMIE and Weimer simulations; however, the Volland-Stern-driven results indicated storm response erosion with a developed drainage plume. Almost all models showed significantly greater plasma densities in the afternoon and postdusk sectors,

leading to a poor match to the EUV-extracted plasmapause in those sectors. All methods performed well for matching in the predawn and morning sectors.

Figure 4 (second row) shows model results after storm onset. The AMIE- and Weimer 96-driven simulations showed the development of the drainage plume. This was indicated by the movement of the plasma trough toward the dayside edge of the simulation domain and deformation of the plasmapause in this direction. Also important was the lack of detection of a plasmapause in the dayside region, which is a common signature of the formation of the drainage plume. The AMIE runs were also the only ones that showed the existence of major secondary structures that extended into the plasma trough region (as evidenced by the density contours not being smooth in the longitudinal direction, especially on the nightside and into the dawn sector).

Three hours later (20:20 UT), all models showed a clearly developed drainage plume, though the size and orientation of these plumes varied significantly. AMIE versions showed "fingers" on the morning/dayside drainage plume (as evidenced by the density contours not being smooth in the longitudinal direction), and both versions showed significantly greater nightside content compared to all other simulations, as was expected by the potential pattern.

Figure 4 (fifth and sixth rows) show the eroded, poststorm plasmasphere. Compared to the initial state, the density contours showed much less content, with the presence of an extended dayside plasma trough. Drainage plumes existed due to the elevated convection in the region, but they were narrower in MLT than in earlier time periods.

There were occasions in which multiple points existed in each longitudinal slice, which was most likely due to the plasmapause having significant structure. If a radial line is followed, the line would go through a constant density contour several times, which could be interpreted as having multiple plasmapause locations. This occurs in the model, as well, but all of the plasmapause identification methods oversimplify this and select only the lowest radial point as the plasmapause. This is obviously a simplification of reality and is a clear limitation of this study.

As part of the analysis, the EUV plasmapause location data were averaged onto the DGCPM grid system for direct comparison. This averaging added in some additional error, where the DGCPM points might have matched some of the plasmapause points, but not all. This effect is demonstrated in Figure 5. In the afternoon and postdusk quadrants the differences between the extracted and averaged data were subtle. In the predawn quadrant, however, the differences were much more drastic, with a span of approximately 2 R_E from the interior to exterior EUV-extracted data points in a radial slice. Note that at other times during the storm, the observed plasmapause extractions are most variable in the afternoon sector due to the plume.

3.3. Plasmapause Comparison

One of the goals for this study was to examine a variety of methods for calculating the plasmapause location and determining an "average best" method in regard to matching EUV plasmapause extractions. The three methods for calculation were described earlier in this paper and are referred to as the "Gradient," "Fitted," and "Saturation" methods. Previous studies, including those that initially detailed the discovery of the plasmapause from whistler observations [*Carpenter*, 1963], made use of the gradient method to identify the plasmapause, and it has been the traditionally accepted method of plasmapause detection. During analysis of these simulations, however, it was found that the gradient method produced poor matches to the EUV data, and other methods were attempted to determine if a better process could be employed for the goal of matching the EUV plasmapause data set.

Figure 6 shows a comparison of these three methods and their differences to the EUV extracted plasmapause data set. In the figure, five different run configurations (AMIE-Mag, AMIE-DMSP, W96, W05, and VS) are shown in the five panels, with the root-mean-square (RMS) difference of the EUV and calculated plasmapause points at each time step plotted. These values were calculated by averaging the EUV plasmapause data points to the same longitudinal resolution as the DGCPM grid, and then calculating the differences where common values existed. For each time step, the differences were squared, a mean was determined, and the square root of this value was taken. A zero value indicates a perfect match between the EUV data and the model.

Overall, the "Fitted" and "Saturation" methods had a lower average RMS difference for the duration of the storm for all five models, with this being most dramatic in the Weimer and Volland-Stern variations. During

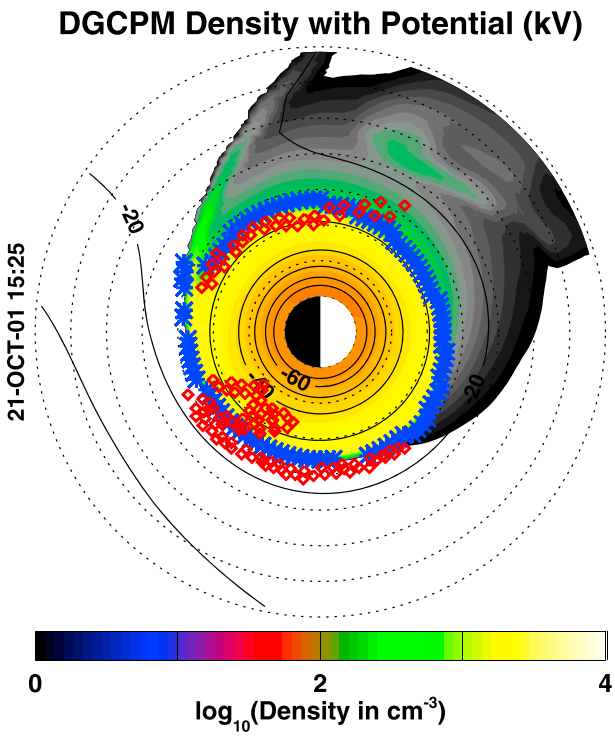

Figure 5. A DGCPM density contour with EUV plasmapause points overlaid, indicating the extracted points as discussed in *Goldstein et al.* [2005] (red) and the DGCPM modeled points using the saturation method (dark blue).

quiet times, these methods had a slightly higher RMS difference that decreased during the course of the storm, meaning the methods were better at representing the storm time, or an eroded plasmasphere, than a quiet time plasmasphere. The "Gradient" method difference was consistently higher than the other methods. The actual values indicated that the gradient method was identifying a peak gradient outside of the EUV-extracted plasmapause points. This was reasonable, however, because these gradients could be either outside the observable range or could occur at low-pixel brightness where they would be harder to identify in the EUV data. The gradient method was successful at identifying this peak gradient, and thus, the definition of the plasmapause, but poor at representing the EUV-derived plasmapause, which was the aim of this study. An alternative explanation could be that the model has a consistent bias such that it is constantly offset from the actual steepest gradient in the real plasmapause. It is difficult to determine whether this is the case without independent observations.

It should also be noted that times when EUV plasmapause points had multiple identified points (as described by *Goldstein et al.* [2005]), the RMS difference increased dramatically. This is a clear limitation of the technique that was developed to identify the plasmapause from the model results. These techniques chose the first radial grid point that satisfied the criteria for identifying the plasmapause, which is obviously incorrect at times. Examining Figure 4 (fourth row), the density contours were consistent with the overall morphology implied by the EUV plasmapause points. This analysis would be more accurate if the plasmapause identification criteria were modified to allow for multiple plasmapause locations for a given MLT sector.

Figure 7 shows the probability distribution function (PDF) of the difference values produced by the three plasmapause detection methods and five different simulations. Some general features can be observed in this figure: (1) the two AMIE-driven models have average errors that are larger than the other electric-field-driven models; (2) the two AMIE-driven model results have a broader range of errors than the other models for the saturation and gradient techniques, as evidenced by the lower peaks and above-zero values at large difference values; (3) the Volland-Stern-driven simulation results have a higher peak than the models driven by other electric fields; and (4) the gradient method most often produced plasmapause points that were farther from the Earth than the EUV measured values, while the fitted and saturation methods produced distributions centered closer to zero.

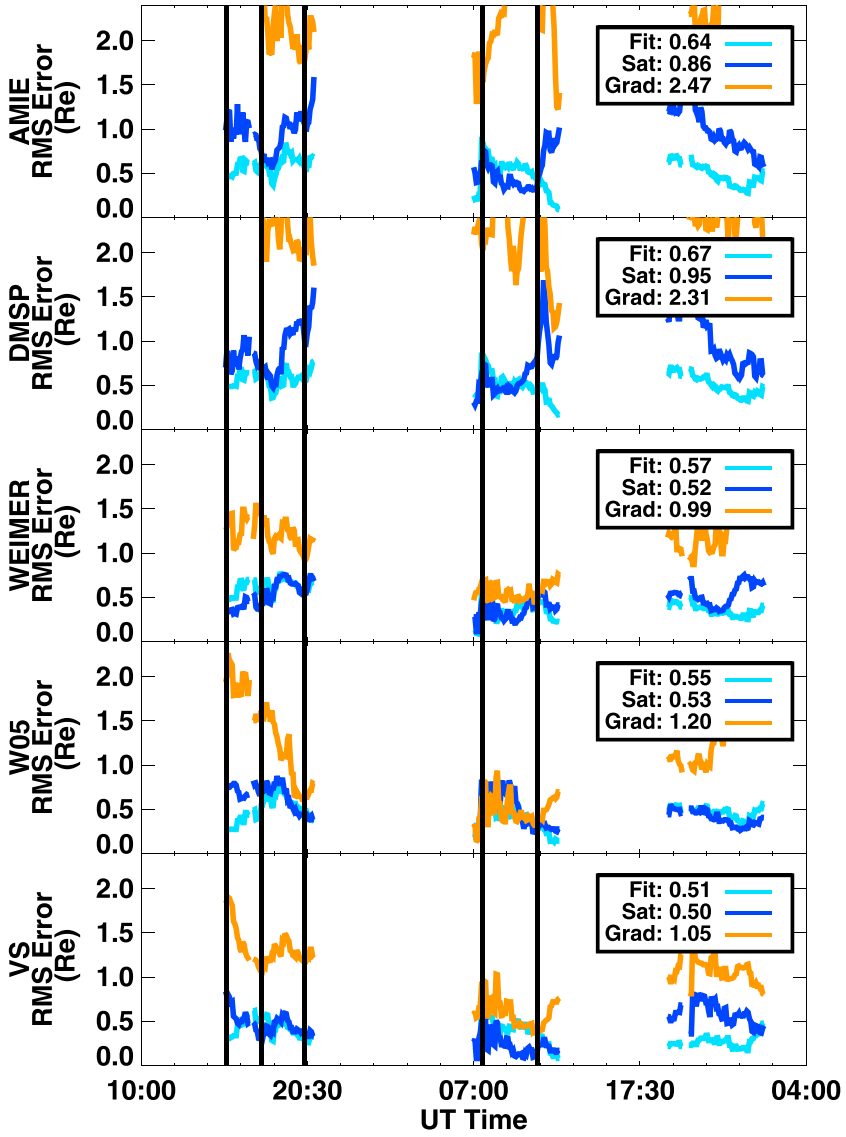

Figure 6. Plots of the RMS error of the three plasmapause detection methods (as described in the paper) applied to the modeled data compared to the extracted EUV plasmapause positions.

4. Other Events

The above analysis was repeated on multiple storms to determine if there were any common trends in the accuracy of the electric field models in reproducing the [*Goldstein et al.*, 2005] described EUV plasmapause extractions. One of the two products of this process was the PDF analysis of Figure 8, which included data from all events used in this study. The same behavior that was observed in the single-event analysis was also observed here: (1) the AMIE-driven model results using the gradient and fitted methods produced some of the largest median errors in the plasmapause location, compared to the other electric field-driven models; (2) the AMIE technique had a broader range of errors for the gradient and fitted methods (i.e., lower peaks and higher percentages for larger differences); (3) the peaks were highest for the Volland-Stern model using the fitted and gradient methods; and (4) the gradient method produced the largest median errors. Table 1 provides a quantitative assessment of these descriptions, providing a root-mean-square error between the measurement and modeled plasmapause position as well as an indication of the percentage of time in which the modeled plasmapause was close to the measured plasmapause (as described below).

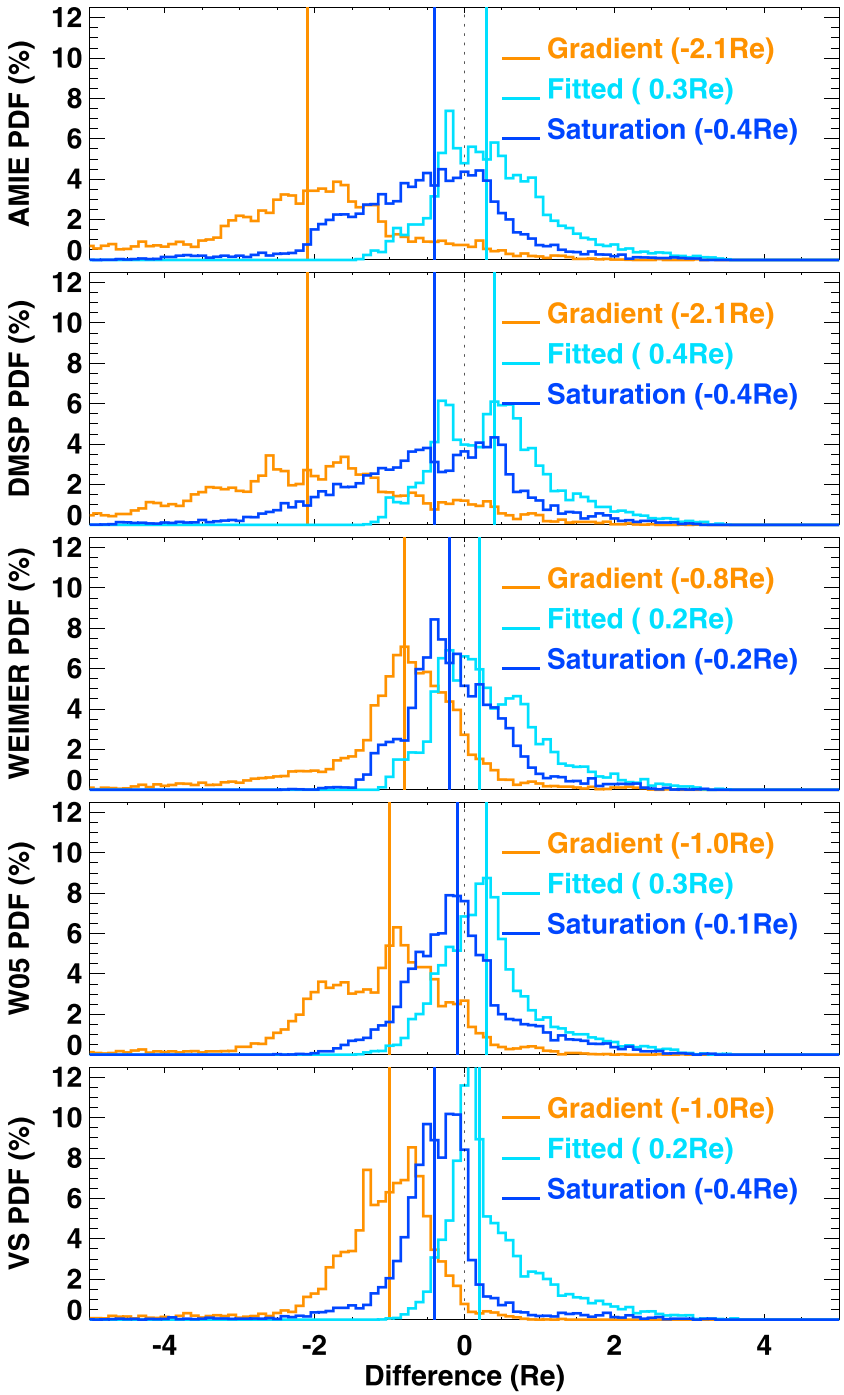

Figure 7. The cumulative PDF function of the error values over the course of the event of 21–23 October 2001, comparing the three plasmapause detection methods applied to the modeled data. Positive values indicate that the EUV plasmapause using the specified method is farther radially from the Earth than the comparative DGCPM simulated plasmapause, and vice versa for negative values. Vertical lines indicate the mean error values; the thin single vertical dotted line assists in identifying zero. The distance values in the labels indicates the median offset error.

Figure 9 shows exactly the same information as Figure 8, but rearranged to explore which plasmapause identification method best matched the extracted EUV points, as described by *Goldstein et al.* [2005]. The fitted technique had a median value of 0.3 *Re* for all of the electric field models and events, since the extracted EUV point locations were used to determine the cutoff value for plasmapause identification. The saturation method had a median error of −0.3 *Re*, or 0.3 *Re* outside, of the extracted EUV plasmapause points. The AMIE

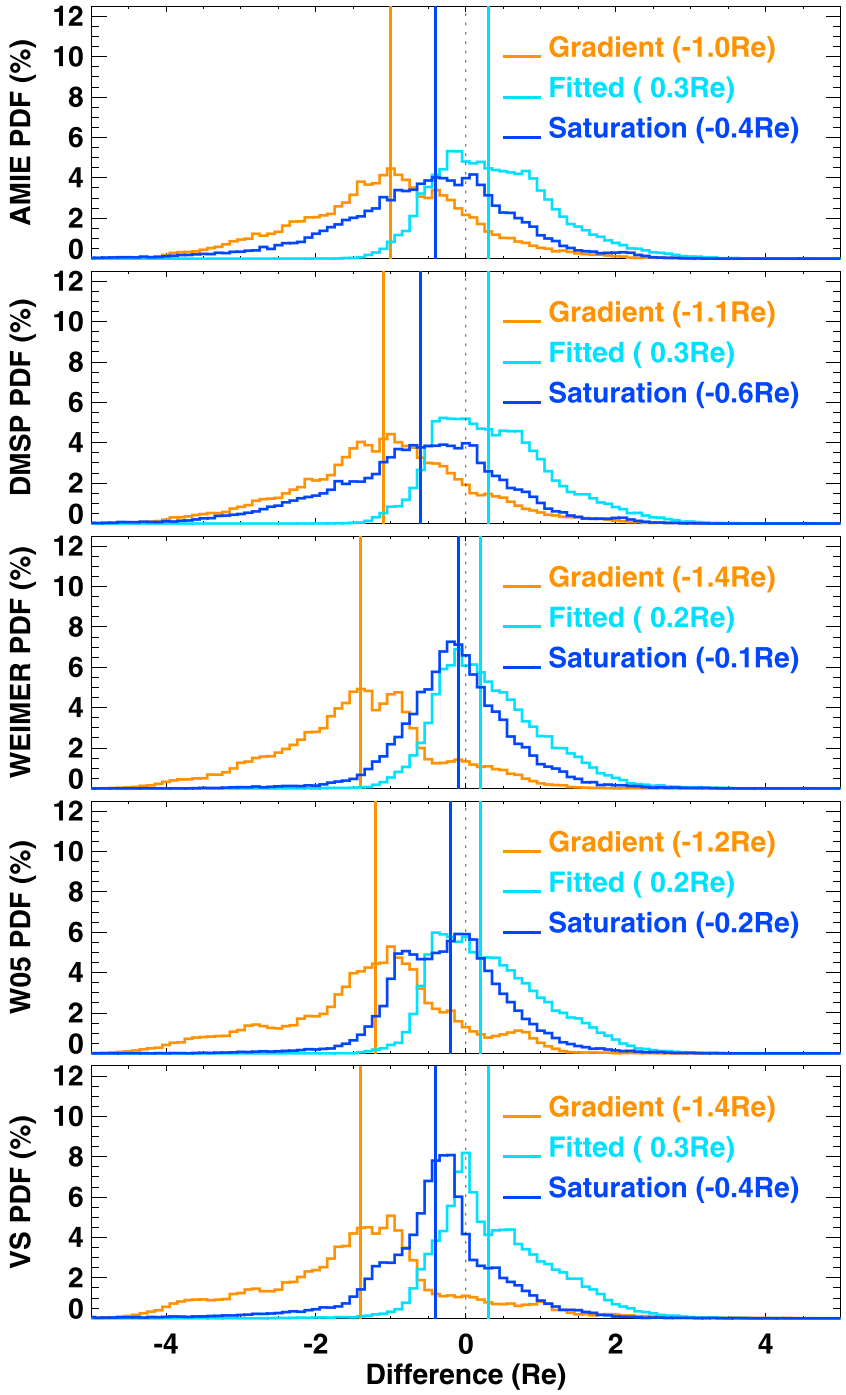

Figure 8. The cumulative PDF of the difference values for each of the three plasmapause detection methods over the course of all the events of this study, as listed by Table 1, in the same format as Figure 7.

technique in the saturation method showed a lower peak and larger percentages at higher differences. The gradient method produced results that were furthest away from the extracted EUV plasmapause locations, with a clear bias of 1.3 *Re* outside the EUV-determined plasmapause.

To put these results in context, a previous study by *Obana et al.* [2010] found that the He^+ and the mass density plasmapause were found collocated within a range of error of ±0.4 *Re*, indicating a rough noise level of detecting the actual plasmapause location. This value was used in this analysis to determine ranges that were considered consistent with EUV observations. The percentages of points within ±0.4 *Re* of zero offset

Table 1. A Comparison of the Efficacy of the Five Different Electric Field Models at Driving the DGCPM, Evaluated by Comparing the Plasmapause Locations Predicted by the Model and Measured by the IMAGE EUV Instrument[a]

Event	*Dst*	Pause	AMIE RMS Error (*Re*)	AMIE Con (%)	DMSP RMS Error (*Re*)	DMSP Con (%)	W96 RMS Error (*Re*)	W96 Con (%)	W05 RMS Error (*Re*)	W05 Con (%)	VS RMS Error (*Re*)	VS Con (%)
3/20/2001	−149	Fit	0.899	56.9	0.848	*65.3*	0.818	65.0	0.798	54.4	0.915	39.3
		Sat	1.405	21.4	1.271	16.2	*0.780*	33.0	0.910	15.4	2.097	6.0
		Grad	2.232	13.5	1.765	15.7	1.341	11.4	1.451	**1.1**	**2.455**	6.9
3/31/2001	−387	Fit	0.791	36.1	0.753	41.6	0.842	36.8	0.898	34.4	0.941	35.0
		Sat	1.074	31.9	1.121	36.1	0.699	*53.4*	*0.635*	52.4	1.144	36.2
		Grad	2.893	5.9	**2.998**	6.1	1.377	18.7	1.549	12.9	1.384	**5.2**
4/11/2001	−271	Fit	0.983	25.7	0.990	26.5	0.871	33.1	0.891	32.0	0.950	34.8
		Sat	1.336	33.9	1.306	34.9	0.934	42.6	0.938	44.6	*0.842*	*49.5*
		Grad	**2.627**	**7.2**	2.601	7.3	1.497	14.8	1.765	12.3	1.771	6.9
4/22/2001	−102	Fit	1.100	29.2	1.068	33.9	0.845	52.1	0.951	36.3	0.915	51.0
		Sat	1.238	31.5	1.434	26.9	*0.644*	*56.7*	0.707	38.1	0.699	51.8
		Grad	2.369	14.7	**2.558**	**9.2**	1.273	34.4	1.576	13.0	1.180	20.8
6/2/2001	−26	Fit	1.002	41.3	1.050	41.0	0.707	44.5	*0.593*	*58.8*	0.976	19.9
		Sat	1.269	23.5	1.285	25.1	1.033	40.7	0.975	46.0	1.022	19.0
		Grad	**2.357**	2.7	2.354	**2.2**	1.558	15.6	1.598	5.3	1.225	19.3
10/21/2001	−187	Fit	0.907	42.3	0.920	37.9	0.843	47.2	0.799	50.5	0.815	*58.4*
		Sat	1.164	32.7	1.271	26.7	*0.690*	47.4	0.758	50.9	0.791	51.2
		Grad	**2.879**	**6.1**	2.775	8.4	1.360	25.9	1.539	17.2	1.392	11.5
11/6/2001	−292	Fit	0.667	48.8	0.663	49.8	0.583	67.6	0.613	65.0	0.555	*73.7*
		Sat	1.402	28.2	1.481	29.4	*0.465*	58.2	0.756	24.3	0.579	57.2
		Grad	3.238	6.1	**3.548**	3.8	1.283	11.6	1.791	**1.5**	1.616	7.1
11/24/2001	−221	Fit	0.800	50.8	0.756	48.7	0.713	47.3	0.750	49.6	0.716	*54.3*
		Sat	1.375	27.8	1.445	23.0	0.715	38.8	0.793	40.3	*0.704*	44.8
		Grad	**3.023**	14.7	2.840	11.6	1.786	16.2	2.845	6.1	2.773	**4.6**
All	N/A	Fit	0.907	38.1	0.907	40.3	0.810	46.5	0.839	43.4	0.855	44.4
		Sat	1.254	30.1	1.312	28.7	*0.754*	*48.1*	0.788	41.8	1.015	42.1
		Grad	**2.694**	9.0	**2.694**	**8.1**	1.420	20.7	1.745	10.5	1.686	10.8

[a]Eight events are shown in this table. In each column the RMS and the consistency between the model run and the EUV data is shown. The consistency is defined as the percentage of the time in which the simulated plasmapause is within 0.4 R_E of the measured plasmapause. For each storm, the modeled plasmapause is identified using the three different techniques, as described in the text. Italic represents the electric field and technique that produced the best result for the given storm, while bold represents the worst performance boxes.

were determined. The fitted method showed the most points within this error bar, with 47.1% of all of the points within ±0.4 *Re* of the EUV identified plasmapause, while the saturation method had less points (41.1%) and the gradient method had the widest and most offset distribution with only 13.1% near zero. It should be noted that there were approximately 75,000 points in each of the distributions for the different electric field drivers, with approximately 350,000 points in the "All" distributions (a sum of all five different electric field model simulations and all eight events).

Table 1 shows the results of this study. Two values are shown: the RMS error, as described above, and the consistency: the percentage of plasmapause points found within 0.4 *Re* of the extracted EUV plasmapause. The highlighted cells refer to the best (italic) and worst (bold) values in each category. The pair of AMIE-driven methods were never the best fit in any simulation type, and in all but one of the simulations represented the worst fit model, as well as being the worst in set of all models. On the other hand, the Weimer variants were often the best, having had the best of either parameter in all but two events, while also having had the best in the set of all models. The Volland-Stern had greater variance with respect to the other models, having been the best in either parameter in four events and the worst in one parameter in three events, similar to the finding of *Liemohn et al.* [2006] regarding the Volland-Stern field's ability to predict plasmaspheric features during storms.

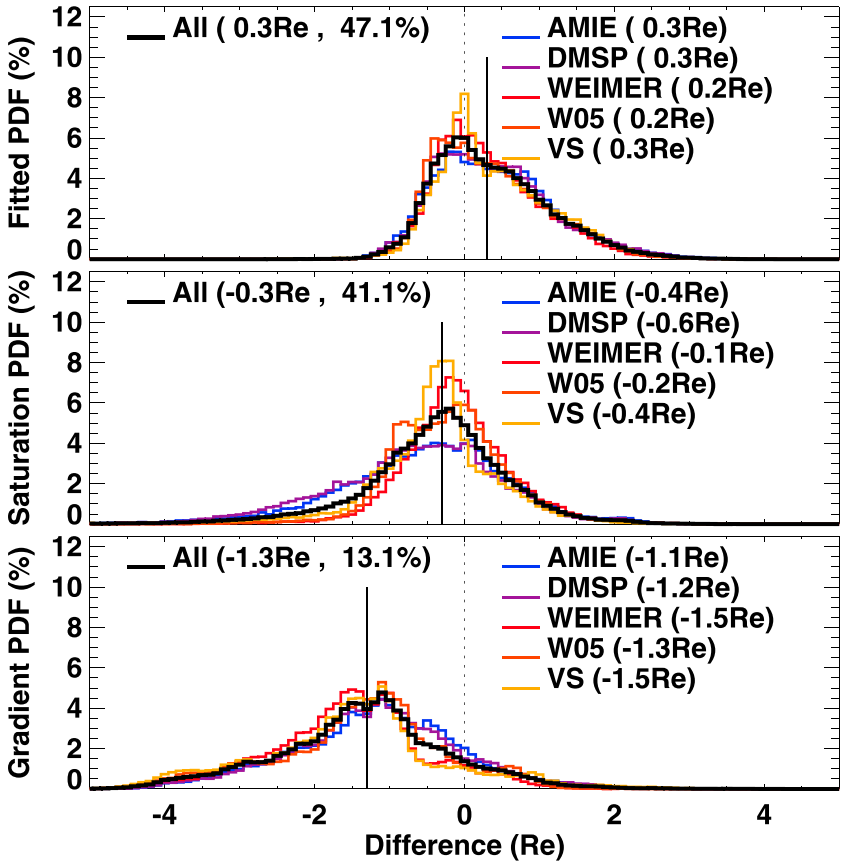

Figure 9. The cumulative PDF functions of the difference values comparing the three plasmapause detection methods over the course of all the events of this study, as listed by Table 1. Positive values indicate that the DGCPM plasmapause using the specified method is farther radially from the Earth than the comparative EUV-measured plasmapause, and vice versa for negative values. The black-lined histogram indicates the average of all of the model results with the different electric fields. The distance values in the labels indicate the median offset error, while the percentage term indicates the percentage of the values that fall within ±0.4 *Re* of zero offset.

The overall differences from the two Weimer variants (W96 and W05) were quite low, and both were better (on average) than the commonly used Volland-Stern method at replicating EUV results, as evidenced by the average values in the bottom three rows of Table 1. All three were close to the minimum expected error, based on previous studies such as those by *Pierrard et al.* [2008] and *Liemohn et al.* [2004]. Both AMIE-driven methods, however, were worse on average using any plasmapause method and produced the most significant deviation from the expected location. This was unexpected, as the AMIE method takes a far greater number of measurements into account when calculating the electric field, compared to either Weimer or Volland-Stern. Other studies that have focused on the high-latitude ionosphere have shown that the AMIE technique is superior to the Weimer models, when compared to DMSP data [*Bekerat et al.*, 2005; *Kihn et al.*, 2006]. It should be noted that the analysis techniques used here (a simple RMS difference) would not allow a quantification of whether AMIE was able to produce the complicated plasmaspheric features such as "bumps," "shoulders," "fingers," and detected plasma bubbles, as expected. An analysis technique that computes the variability of plasmaspheric density as a function of magnetic local time may be useful in quantifying different electric field's ability to produce these features but is beyond the scope of the current study.

5. Discussion

The interpretation of the results presented in Table 1 was that the two Weimer models produced a more accurate representation of the plasmasphere morphology and evolution during the storm events than either AMIE configuration or the Volland-Stern electric field model. This is consistent with previous studies

[*Liemohn et al.*, 2004], which had shown that the *Weimer* [1996] model is reliable at driving plasmaspheric dynamics. There are numerous explanations for this, with the most basic being that the Weimer models better represent subauroral ionospheric features that are not captured in the relatively simple two-cell-driven Volland-Stern model and that are exaggerated due to the assumptions of the AMIE method. The Weimer models are also driven by IMF conditions, allowing their response to be dictated by the temporal resolution of the input IMF data, rather than being forced to a 3 h cadence as is done in *Kp*, and thus leading to an improved plasmasphere during storm onset. Temporal differences in terms of hours have a significant effect on the evolution of large-scale features such as the drainage plume, as well as smaller notch and shoulder features. While Figures 3 and 4 both demonstrated differences between the W96 and W05 models, Table 1 shows the variations between the two models are much smaller than the variations between the other methods. It should be noted that *Weimer* [2001] introduced a lower boundary condition that may have made the electrodynamics slightly less robust within the plasmasphere region, but the differences in our study were quite small.

A key result of this study was that the AMIE-driven results were the least reliable at reproducing plasmaspheric morphology. This was unanticipated, as it was assumed the greater specificity of this electric field description, through the use of numerous magnetometer and DMSP measurements in its calculation, would result in a more accurate plasmasphere representation. The reason for this inconsistency is most likely related to the fact that the majority of the data that went into the AMIE technique were ground-based magnetometer data. At high latitudes, the Hall current causes the majority of the perturbation [e.g., *Yu et al.*, 2010, and references within]. This is due to the fact that if the magnetic fields are radial and there are no gradients in the conductances, the magnetic perturbations on the ground caused by the field-aligned and Pedersen currents will cancel each other [*Fukushima*, 1969]. At lower latitudes, though the ground-based magnetic perturbations are influenced not only by the Hall current but the Pedersen, field-aligned and magnetospheric currents as well [*Yu et al.*, 2010]. The AMIE technique makes the assumption that the magnetic perturbations are only caused by Hall currents. AMIE can subtract the magnetospheric current of the magnetic perturbations by calculating the *Dst* index and applying a latitudinal correction. This does not remove the field-aligned and Pedersen currents, though. So it is expected that AMIE should work best at higher latitudes while, at lower latitudes (which map to the plasmasphere), the potentials might not be as accurate. Further, the data that go into AMIE becomes more sparse at lower latitudes. This is because the physical distance between measurement points becomes larger at lower latitudes (i.e., there is less area in the polar cap than in the subauroral region), and there are large areas in which there are no ground-based magnetometers at subauroral latitudes. Adding the DMSP data should, in theory, help with the AMIE patterns, but statistically it does not help much. This is because the DMSP data are quite sparse in longitude, and therefore, the AMIE patterns are not influenced very much (in the global sense) by the data at subauroral latitudes.

This study presents three different methods for determining the plasmapause location within a model of the plasmasphere. These locations are compared to plasmapause locations extracted from EUV images, as described by *Goldstein et al.* [2005]. Since the plasmapause is the location of a sharp dropoff in the plasma density, it was expected that the best method to determine the plasmapause location in the model results would be a method based on the gradients in the plasma density. This turned out not to be the case. Instead, the gradient method produced the worst results, while using a constant threshold density value produced much better results. An additional method, based on determining where the model density was significantly below the saturation density, also showed better performance than the gradient method. This leads to two possible conclusions: (1) the DGCPM does not model the steepest gradients in the plasmasphere very accurately or (2) the method of plasmapause extraction described by *Goldstein et al.* [2005] does not describe the steepest gradient in the plasmasphere but instead identifies either a constant density or the location in which there occurs a significant decrease in density compared to an "expected" value of the plasmaspheric density. Without an independent method of validating the model results and the EUV extraction points, it is impossible to determine which conclusion is more likely.

A result of this study seemingly conflicts with a result of the *Liemohn et al.* [2004] study. In that study, it was argued that a single-density isocontour did not correspond well with the plasmapause points found by the IMAGE EUV. The fitted plasmapause-detection method employed in this study, however, was shown to match the plasmapause with a reasonably high accuracy. It was expected that the mean difference between the EUV and the modeled plasmapause would be close to zero in the present study, though since the

density threshold was determined by comparing the location of the plasmapause in the EUV data to the density levels in the simulation results. Moreover, the "observed" plasmapause locations were extracted by eye from EUV images that had a monochromatic color scale, potentially biasing these values to be clustered near a certain count rate (i.e., density) value.

The success of the saturation method at representing the plasmapause position was an interesting development. While there is not a clear explanation for this, it may be related to the fact that the plasmapause lies close to (though not necessarily collocated with) the open-closed flow line separatrix prior to the storm. Around this separatrix location, flow lines transition from closed drift paths, in which the field lines are saturation limited, to open flow lines that are allowed to empty freely through the magnetopause, so that the difference between the actual density and the saturation density is quite large. This causes a large gradient in the plasmaspheric saturation level that appears to be close to the location of the EUV brightness cutoff that was identified as the plasmapause boundary. An additional reason why this method might compare well to the EUV-extracted data points is that the saturation method identifies the location in which the density in the model drops below an expected value. If one were identifying a boundary from images by eye, one might choose the location in which the density drops below an expected value. When looking at a series of images, it is easy to see when the value of density grows or decreases away from the value that is expected. Therefore, it is relatively easy to understand how identifying locations in which the modeled density drops below the saturation density (or expected density) may match the boundaries identified by eye from images.

6. Conclusion

A comparative study was undertaken to examine the efficacy of five different electric field models in driving a plasmaspheric model during eight storm events. It was found that the *Weimer* [1996, 2005] potential patterns were particularly good at driving the model to match manually extracted IMAGE EUV plasmapause locations. The Volland-Stern-driven model also produced results that correctly described the bulk evolution of the plasmasphere when compared with the EUV data, yet it was hindered by the reliance of *Kp* data as a driving input method. *Kp* data have an insufficient temporal resolution to accurately describe the plasmaspheric response at storm onset and may produce a plasmasphere response that is offset from the realistic response by a matter of hours. AMIE potential patterns were a poor driver of the model when compared to the EUV-derived plasmapause for all storm events, most like due to the limitations of using low-latitude magnetometer measurements to determine the electric potential. While no model consistently produced results within the desired accuracy of 0.4 R_E of the EUV-obtained plasmapause location, the Weimer models most consistently approached this value.

The fitted and saturation methods produced the most accurate matching to the EUV-derived plasmapause points when compared with the more commonly used gradient method. While the fitted and saturation methods have the same magnitude of their median offset (0.3 *Re*), the distribution of the fitted method has more points near zero, though the saturation method does not need to estimate an optimum density contour to use as the boundary location, as the fitted method does.

Acknowledgments

This research was funded by National Science Foundation grant ATM1010812 as well as Air Force Office of Scientific Research grants FA9550-12-1-0401 and FA9550-12-1-0265. The authors would like to thank the IMAGE EUV science team for providing the plasmapause locations throughout these storm periods. Roxanne Katus provided the IMAGE EUV data mapped to the equatorial plane. We acknowledge use of NASA/GSFC's Space Physics Data Facility's OMNIWeb service, and OMNI data for the solar wind and interplanetary magnetic field data. For the AMIE simulations, significant amounts of data were used: the Canadian Space Agency provided most of the data in the lower latitude Canadian sector; the IMAGE magnetometer network is a joint enterprise between a number of European Institutes and provides very dense coverage over the entire European continent; the MACCS project was a joint venture between the Augsburg College Physics Department and Boston University's Astronomy Department to study natural interactions in the Earth's space environment; the 210 Magnetic Meridian observations are being conducted by Kyushu University, and the database and archives are being maintained by STEL, Nagoya University; the Greenland Coastal Stations were operated by the Danish Meteorological Institute (DMI); the Magnetometer Array on the Greenland Ice Cap (MAGIC) magnetometers were operated by the University of Michigan's Magnetosphere-Ionosphere Science Team; the INTERMAGNET programme exists to establish a global network of cooperating digital magnetic observatories, adopting modern standard specifications for measuring and recording equipment, in order to facilitate data exchanges and the production of geomagnetic products in close to real time; and the DMSP data were provided by Marc Hairston at University of Texas, Dallas.

Larry Kepko thanks the reviewers for their assistance in evaluating this paper.

References

Bekerat, H., R. Schunk, L. Scheirles, and A. Ridley (2005), Comparison of satellite ion drift velocities with AMIE derived convection patterns, *J. Atmos. Sol. Terr. Phys.*, *67*, 1463–1479.

Borovsky, J. E., and M. H. Denton (2006), Effect of plasmaspheric drainage plumes on solar-wind/magnetosphere coupling, *Geophys. Res. Lett.*, *33*, L20101, doi:10.1029/2006GL026519.

Borovsky, J. E., and M. H. Denton (2008), A statistical look at plasmaspheric drainage plumes, *J. Geophys. Res.*, *113*, A09221, doi:10.1029/2007JA012994.

Carpenter, D., and R. R. Anderson (1992), An ISEE/whistler model of equatorial electron density in the magnetosphere, *J. Geophys. Res.*, *97*, 1097–1108.

Carpenter, D. L. (1963), Whistler evidence of a 'knee' in the magnetospheric ionization density profile, *J. Geophys. Res.*, *68*, 1675–1682, doi:10.1029/JZ068i006p01675.

Carpenter, D. L., and J. Lemaire (1997), Erosion and recovery of the plasmasphere in the plasmapause region, *Space Sci. Rev.*, *102*, 153–179, doi:10.1023/A:1004981919827.

Carpenter, D. L., and C. G. Park (1973), On what ionospheric workers should know about the plasmapause-plasmasphere, *Rev. Geophys. Space Phys.*, *11*, 133–154, doi:10.1029/RG011i001p00133.

Darrouzet, F., et al. (2008), Plasmaspheric density structures and dynamics: Properties observed by the Cluster and Image missions, *Space Sci. Rev.*, *145*, 55–106, doi:10.1007/s11214-008-9438-9.

Dent, Z. C., I. R. Mann, J. Goldstein, F. W. Menk, and L. G. Ozeke (2006), Plasmaspheric depletion, refilling, and plasmapause dynamics: A coordinated ground-based and image satellite study, *J. Geophys. Res.*, *111*, A03205, doi:10.1029/2005JA011046.

Foster, J., J. Holt, R. Musgrove, and D. Evans (1986), Ionospheric convection associated with discrete levels of particle precipitation, *Geophys. Res. Lett.*, *13*, 656–659.
Foster, J. C. (2004), Stormtime observations of the flux of plasmaspheric ions to the dayside cusp/magnetopause, *Geophys. Res. Lett.*, *31*, L08809, doi:10.1029/2004GL020082.
Fukushima, N. (1969), Equivalence in ground geomagneitc effect of Chapman-Vestine's and Birkland-Alfven's electric current-systems for polar magnetic storms, *Rep. Ionos. Space Res. Jpn.*, *23*(3), 219–227.
Goldstein, J. (2003), Identifying the plasmapause in IMAGE EUV data using IMAGE RPI in situ steep density gradients, *J. Geophys. Res.*, *108*(A4), 1147, doi:10.1029/2002JA009475.
Goldstein, J., B. R. Sandel, W. T. Forrester, M. F. Thomsen, and M. R. Hairston (2005), Global plasmasphere evolution 22–23 April 2001, *J. Geophys. Res.*, *110*, A12218, doi:10.1029/2005JA011282.
Grebowsky, J. M. (1970), Model study of plasmapause motion, *J. Geophys. Res.*, *75*, 4329–4333, doi:10.1029/JA075i022p04329.
Gringauz, K. I., V. G. Kurt, V. I. Moroz, and I. S. Shklovskii (1961), Results of observations of charged particles observed out to R = 100, 000 km, with the aid of charged-particle traps on Soviet Space Rockets, *Soviet Astron.*, *4*, 680.
Horwitz, J., S. Menteer, J. Turnley, J. Burch, J. Winningham, C. Chappell, J. Craven, L. Frank, and D. Slater (1986), Plasma boundaries in the inner magnetosphere, *J. Geophys. Res.*, *91*, 8861–8882.
Horwitz, J. L., R. H. Comfort, P. G. Richards, M. O. Chandler, C. R. Chappell, P. Anderson, W. B. Hanson, and L. H. Brace (1990), Plasmasphere-ionosphere coupling. II—Ion composition measurements at plasmaspheric and ionospheric altitudes and comparison with modeling results, *J. Geophys. Res.*, *95*, 7949–7959, doi:10.1029/JA095iA06p07949.
Kennel, C. F., and H. E. Petschek (1966), Limit on stably trapped particle fluxes, *J. Geophys. Res.*, *71*(1), 1–28.
Kihn, E. A., R. Redmon, A. J. Ridley, and M. R. Hairston (2006), A statistical comparison of the AMIE derived and DMSP-SSIES observed high-latitude ionospheric electric field, *J. Geophys. Res.*, *111*, A08303, doi:10.1029/2005JA011310.
Lemaire, J., and K. Gringauz (1998), *The Earth's Plasmasphere*, chap. 4.2, Cambridge Univ. Press, Cambridge, U. K.
Liemohn, M., A. Ridley, D. Gallagher, D. Ober, and J. Kozyra (2004), Dependence of plasmaspheric morphology on the electric field description during the April 17, 2002 magnetic storm, *J. Geophys. Res.*, *109*, A03209, doi:10.1029/2003JA010304.
Liemohn, M. W., A. J. Ridley, J. U. Kozyra, D. L. Gallagher, M. F. Thomsen, M. G. Henderson, M. H. Denton, P. C. Brandt, and J. Goldstein (2006), Analyzing electric field morphology through data-model comparisons of the Geospace Environment Modeling Inner Magnetosphere/Storm Assessment Challenge events, *J. of Geophys. Res.*, *111*, A11S11, doi:10.1029/2006JA011700.
Lyons, L. R., and R. M. Thorne (1973), Equilibrium structure of radiation belt electrons, *J. Geophys. Res.*, *78*, 2142–2149, doi:10.1029/JA078i013p02142.
Matsui, H., P. A. Puhl-Quinn, J. W. Bonnell, C. J. Farrugia, V. K. Jordanova, Y. V. Khotyaintsev, P.-A. Lindqvist, E. Georgescu, and R. B. Torbert (2010), Characteristics of storm time electric fields in the inner magnetosphere derived from Cluster data, *J. Geophys. Res.*, *115*, A11215, doi:10.1029/2010JA015450.
Maynard, N. C., and A. J. Chen (1975), Isolated cold plasma regions: Observations and their relation to possible production mechanisms, *J. Geophys. Res.*, *80*, 1009–1013, doi:10.1029/JA080i007p01009.
Moldwin, M. B. (1997), Outer plasmaspheric plasma properties: What we know from satellite data, *Space Sci. Rev.*, *80*, 181–198, doi:10.1023/A:1004921903897.
Moldwin, M. B., S. Mayerberger, H. K. Rassoul, T. Barnicki, and R. R. Anderson (2003a), Plasmapause response to geomagnetic storms: CRRES results, *J. Geophys. Res.*, *108*, 1399, doi:10.1029/2003JA010187.
Moldwin, M. B., B. R. Sandel, M. F. Thomsen, and R. C. Elphic (2003b), Quantifying global plasmaspheric images with in situ observations, *Space Sci. Rev.*, *109*, 47–61, doi:10.1023/B:SPAC.0000007512.69979.8f.
Obana, Y., G. Murakami, I. Yoshikawa, I. R. Mann, P. J. Chi, and M. B. Moldwin (2010), Conjunction study of plasmapause location using ground-based magnetometers, IMAGE-EUV, and Kaguya-TEX data, *J. Geophys. Res.*, *115*, A06208, doi:10.1029/2009JA014704.
Ober, D., J. L. Horwitz, and D. L. Gallagher (1997), Formation of density troughs embedded in the outer plasmasphere by subauroral ion drift events, *J. Geophys. Res.*, *102*(A7), 14,595–14,602.
Ozeke, L. G., and I. R. Mann (2008), Energization of radiation belt electrons by ring current ion driven ULF waves, *J. Geophys. Res.*, *113*, A02201, doi:10.1029/2007JA012468.
Pierrard, V., G. V. Khazanov, J. Cabrera, and J. Lemaire (2008), Influence of the convection electric field models on predicted plasmapause positions during magnetic storms, *J. Geophys. Res.*, *113*, A08212, doi:10.1029/2007JA012612.
Rasmussen, C., S. M. Guiter, and S. G. Thomas (1993), Two-dimensional model of the plasmasphere: Refilling time constants, *Planet. Space Sci.*, *41*, 35–43.
Rich, F., and M. Hairston (1994), Large-scale convection patterns observed by DMSP, *J. Geophys. Res.*, *99*, 3827–3844.
Richmond, A., and Y. Kamide (1988), Mapping electrodynamic features of the high-latitude ionosphere from localized observations: Technique, *J. Geophys. Res.*, *93*, 5741–5759.
Ridley, A. (2000), Estimation of the uncertainty in timing the relationship between magnetospheric and solar wind processes, *J. Atmos. Sol. Terr. Phys.*, *62*, 757–771.
Ridley, A., and E. Kihn (2004), Polar cap index comparisons with AMIE cross polar cap potential, electric field, and polar cap area, *Geophys. Res. Lett.*, *31*, L07801, doi:10.1029/2003GL019113.
Roelof, E. C., and A. J. Skinner (2000), Extraction of ion distributions from magnetospheric ENA and EUV images, *Space Sci. Rev.*, *91*, 437–459.
Sandel, B. R. (2011), Composition of the plasmasphere and implications for refilling, *Geophys. Res. Lett.*, *38*, L14104, doi:10.1029/2011GL048022.
Sandel, B. R., J. Goldstein, D. L. Gallagher, and M. Spasojevic (2003), Extreme ultraviolet imager observations of the structure and dynamics of the plasmasphere, *Space Sci. Rev.*, *109*, 25–46, doi:10.1023/B:SPAC.0000007511.47727.5b.
Sandel, W. R., R. A. King, W. T. Forrester, D. L. Gallagher, C. C. Curtis, and A. L. Broadfoot (2000), An overview of image EUV observations of the plasmasphere, *Eos Trans. AGU*, *81*, Fall Meet. Suppl. F1033.
Shprits, Y. Y., R. M. Thorne, R. B. Horne, S. A. Glauert, M. Cartwright, C. T. Russell, D. N. Baker, and S. G. Kanekal (2006), Acceleration mechanism responsible for the formation of the new radiation belt during the 2003 halloween solar storm, *Geophys. Res. Lett.*, *33*, L05104, doi:10.1029/2005GL024256.
Sojka, J. J., C. E. Rasmussen, and R. W. Schunk (1986), An interplanetary magnetic field dependent model of the ionospheric convection electric field, *J. Geophys. Res.*, *91*(A10), 11,281–11,290, doi:10.1029/JA091iA10p11281.
Spasojević, M. (2003), Global response of the plasmasphere to a geomagnetic disturbance, *J. Geophys. Res.*, *108*, 1340, doi:10.1029/2003JA009987.
Stern, D. (1975), The motion of a proton in the equatorial magnetosphere, *J. Geophys. Res.*, *80*, 595–599.

Stone, E., A. Frandsen, R. Mewaldt, E. Christian, D. Margolies, J. Ormes, and F. Snow (1998), The advanced composition explorer, *Space Sci. Rev.*, *1*, 1–22, doi:10.1023/A:1005082526237.

Summers, D., R. M. Thorne, and F. Xiao (1998), Relativistic theory of wave-particle resonant diffusion with application to electron acceleration in the magnetosphere, *J. Geophys. Res.*, *103*, 20,487–20,500, doi:10.1029/98JA01740.

Tóth, G., et al. (2005), Space weather modeling framework: A new tool for the space science community, *J. Geophys. Res.*, *110*, A12226, doi:10.1029/2005JA011126.

Tóth, G., et al. (2012), Adaptive numerical algorithms in space weather modeling, *J. Comput. Phys.*, *231*, 870–903, doi:10.1016/j.jcp.2011.02.006.

Volland, H. (1973), A semiempirical model of large-scale magnetospheric electric fields, *J. Geophys. Res.*, *78*, 171–180, doi:10.1029/JA078i001p00171.

Weimer, D. (1996), A flexible, IMF dependent model of high-latitude electric potential having "space weather" applications, *Geophys. Res. Lett.*, *23*, 2549–2552.

Weimer, D. (2001), An improved model of ionospheric electric potentials including substorm perturbations and application to the Geosphace Environment Modeling November 24, 1996, event, *J. Geophys. Res.*, *106*, 407-416.

Weimer, D. R. (2005), Improved ionospheric electrodynamic models and application to calculating Joule heating rates, *J. Geophys. Res.*, *110*, A05306, doi:10.1029/2004JA010884.

Yu, Y., A. Ridley, D. Welling, and G. Tóth (2010), Including gap-region field-aligned currents and magnetospheric currents in the MHD calculation of ground-based magnetic field perturbations, *J. Geophys. Res.*, *115*, A08207, doi:10.1029/2009JA014869.

Zong, Q.-G., X.-Z. Zhou, Y. F. Wang, X. Li, P. Song, D. N. Baker, T. A. Fritz, P. W. Daly, M. Dunlop, and A. Pedersen (2009), Energetic electron response to ULF waves induced by interplanetary shocks in the outer radiation belt, *J. Geophys. Res.*, *114*, A10204, doi:10.1029/2009JA014393.